

See discussions, stats, and author profiles for this publication at: <https://www.researchgate.net/publication/339358275>

Visible Light CO₂ Reduction to CH₄ Using Hierarchical Yolk@shell TiO₂-xHx Modified with Plasmonic Au-Pd Nanoparticles

Article in ACS Sustainable Chemistry & Engineering · February 2020

DOI: 10.1021/acssuschemeng.9b06751

CITATIONS

0

READS

51

5 authors, including:



Abolfazl Ziarati

University of Geneva

43 PUBLICATIONS 447 CITATIONS

[SEE PROFILE](#)



Alireza Badiei

University of Tehran

425 PUBLICATIONS 4,576 CITATIONS

[SEE PROFILE](#)



Rafael Luque

University of Cordoba (Spain)

649 PUBLICATIONS 15,317 CITATIONS

[SEE PROFILE](#)

Some of the authors of this publication are also working on these related projects:



Project Green Technologies for the Environment [View project](#)



Project MFC Based Biosensors [View project](#)

Visible Light CO₂ Reduction to CH₄ Using Hierarchical Yolk@shell TiO_{2-x}H_x Modified with Plasmonic Au–Pd Nanoparticles

Abolfazl Ziarati, Alireza Badiei, Rafael Luque, Massoud Dadras, and Thomas Burgi*



Cite This: <https://dx.doi.org/10.1021/acssuschemeng.9b06751>



Read Online

ACCESS |

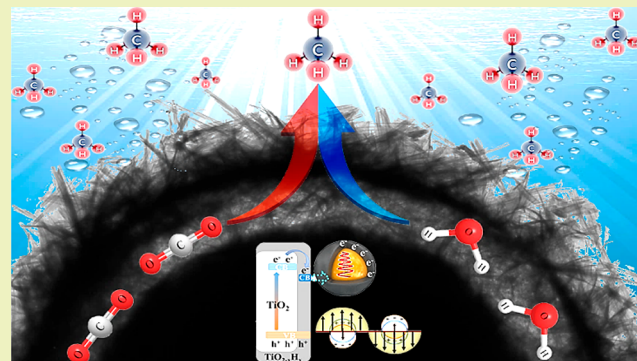
Metrics & More

Article Recommendations

Supporting Information

ABSTRACT: Engineering of advanced semiconductor photocatalysts for CO₂ conversion to solar fuels is a promising strategy to solve the greenhouse effect and energy crisis. Herein, hierarchical urchin-like yolk@shell TiO_{2-x}H_x decorated with core/shell Au–Pd plasmonic nanoparticles (HUY@S-TOH/AuPd) have been prepared using a multistep process and are employed as an advanced visible light active photocatalyst in CO₂ conversion to CH₄ with a rate of 47 μmol/g_{cat}·h (up to 126 μmol/g_{cat} after 7 h). Different engineered sites in this structure for high gas adsorption, powerful visible light activation, and intense electron transportation are responsible for the observed high photocatalytic CO₂ conversion efficiency. The present smart design process can produce considerable cooperation in not only disclosing the architectural engineering for the improvement of photoconversion efficiency but also disclosing it as a viable and appropriate photocatalytic process to sustainable energy production.

KEYWORDS: CO₂ conversion, Photocatalysis, Nanoarchitecture, Oxygen vacancy, Plasmonic nanoparticles



INTRODUCTION

The replacement of fossil energy and the greenhouse effect will be two main challenges for mankind in the near future.¹ Photoreduction of CO₂ in the presence of water to hydrocarbon fuels has gained significant interest in recent years since it would help to decrease atmospheric CO₂ and eventually contribute to the ever growing fuel and energy demand.^{2–4} These aims can be accomplished by the design of advanced semiconductor photocatalysts.^{5,6}

In this regard, titanium dioxide (TiO₂) is one of the most promising semiconductors, due to its considerable photoactivity and stability.⁷ Nevertheless, this semiconductor has some limitations that have to be overcome to become a highly active photocatalyst. The wide band gap of TiO₂ restricts the activity to the ultraviolet (UV) region. The smooth surface of common TiO₂ nanoparticles disfavors high light harvesting. Moreover, the low surface area and nonporosity of commercial TiO₂ leads to poor adsorption properties, especially for gases. All of these obstacles have led to low photocatalytic CO₂ conversion efficiency using pristine TiO₂ as a photocatalyst.^{8,9}

It has been convincingly shown that the engineering of TiO₂ architectures has considerable effects on its photocatalytic efficiency.^{10,11} Yolk@shell (Y@S) structures, as a special class of core–shell configuration with unique core@void@shell frameworks, have gained wide attention due to their ability for specific applications. The existence of the porous hollow shell and the free interior void endows the yolk@shell structures

with high surface area and great adsorption ability for reactants.^{12,13} Therefore, this architecture has significant potential for photocatalytic CO₂ conversion, since the adsorption and trapping of CO₂ on the photocatalyst sites is the first critical step for the CO₂ photoreduction reaction.^{14,15}

To further develop yolk@shell nanostructures, we have suggested a type of this morphology with hierarchical urchin-like structure. Hierarchical urchin-like Y@S architectures have advantages over the smooth Y@S morphology because of their higher specific surface area and increased light harvesting ability. A high specific surface area contributes to the generation and migration of photocarriers and the absorption of CO₂ and H₂O in the structure. Moreover, the hierarchical surface is another advantage of the urchin-like Y@S structure that could bring about improved light-activated photocatalytic sites due to the absorption, reflection, and scattering of light between the needles on the surface of urchin-like structure in addition to the inner yolk–shell void space.^{16,17}

However, the challenge concerning the large band gap and consequently the lacking visible activity of TiO₂ still need to be addressed. It has recently been shown that hydrogenated black

Received: November 12, 2019

Revised: January 16, 2020

Published: February 18, 2020

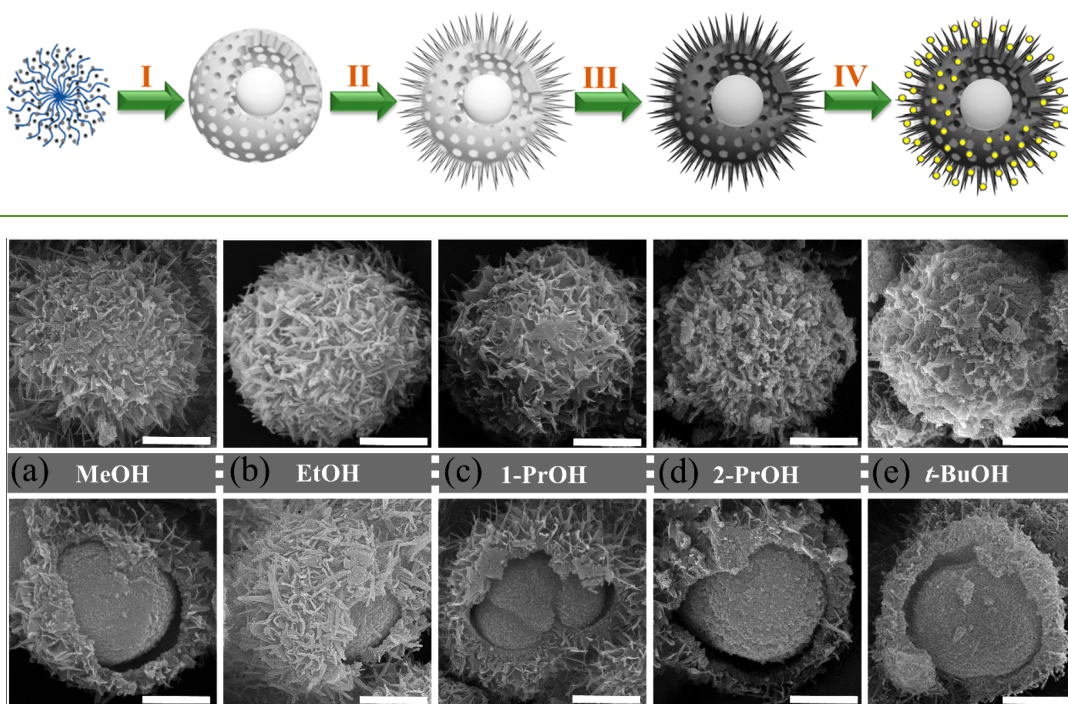
Scheme 1. Schematic Illustration of the Morphological Evolution of Designed Photoactive Systems

Figure 1. SEM images illustrating the effect of the dissolution–renucleation process on the surface of Y@S TiO₂ in the presence of MeOH (a), EtOH (b), 1-PrOH (c), 2-PrOH (d), and *t*-BuOH (e). The scale bars are 1 μm.

TiO₂ (TiO_{2-x}H_x) displays considerably improved visible light response as compared to conventional TiO₂.^{18–20} The properties of TiO_{2-x}H_x are attributed to the thin disordered surface layer created in the hydrogenation process.^{21,22} The synergistic effect between oxygen vacancies and structural defects in this disordered layer is the narrowing of the TiO₂ band gap to the visible region.^{23,24} Moreover, surface defects can provide excess electrons and adsorption sites for CO₂ and H₂O molecules.^{25,26}

On the other hand, it is generally accepted that noble metals create electron sinks and active sites for photocatalytic CO₂ conversion.^{27,28} Decoration of semiconductor structures with noble metals is an attractive way to reduce charge recombination, increasing the visible light activity as well as enriching electron-mediated transportations for enhanced CO₂ photoreduction.²⁹ Au–Pd bimetallic nanoparticles are one of the best candidates due to their excellent photocatalytic activity, especially in conjugation with semiconductor structures. In the presence of light, electrons can transfer from the conductive band of the semiconductor to the attached Au–Pd bimetallic nanoparticles.³⁰ Additionally, due to the strong local surface plasmon resonance (LSPR) in Au nanoparticles, the visible light can excite hot electrons from Au which are injected into adjacent Pd nanoparticles.³¹ Thus, the electron-rich palladium on the surface of the photocatalyst can efficiently reduce CO₂ under visible light irradiation.³²

Based on these premises and in continuation with research endeavors from our groups,^{14,33–35} herein, hydrogenated TiO₂ with a hierarchical urchin-like yolk@shell structure decorated by Au–Pd bimetallic nanoparticles has been designed for photocatalytic CO₂ reduction to solar fuels. The size and shape of the hierarchical needles on the urchin-like structure were fine-tuned by adjusting the type of alcohol during the alkaline dissolution–renucleation process. This structure is rationally

engineered for high gas adsorption, powerful visible light activity, and favorable electron transports. In this superstructure, CO₂ and H₂O can adsorb not only in the porous urchin-like Y@S structure but also in the surface defect sites generated during hydrogen treatment. Oxygen vacancies on the surface of the structure as well as the Au–Pd plasmonic nanoparticles in contact with the semiconductor are responsible for visible activity. Ti³⁺ species can further provide photogenerated electrons upon visible light irradiation to enrich the electron density of decorated Au–Pd nanoparticles. Meanwhile, the produced hot electrons in Au nanoparticles, caused by LSPR, can be injected into the palladium shell to progress the CO₂ reduction reaction. The contribution of different engineered sites in the designed HUY@S-TOH/AuPd photocatalyst leads to synergistic effects that are favorable in the photoreduction of CO₂ to CH₄.

RESULTS AND DISCUSSION

Preparation and Characterization of HUY@S-TOH/AuPd Architecture. The HUY@S-TOH/AuPd prepared based on our recently reported process comprises the following sequential steps³⁵ (Scheme 1): (I) production of Y@S-TO in solvothermal reaction, (II) preparation of Y@S-TO with a hierarchically urchin-like shell (HUY@S-TO) under dissolution–renucleation procedure in alkaline water/alcohol media, (III) hydrogenation of the as-prepared structure to obtain HUY@S-TOH architectures under a high-temperature hydrogen treatment process, (IV) fabrication of Au–Pd core/shell nanoparticles using oleylamine, and decoration of prepared plasmonic Au–Pd nanoparticles on the surface of HUY@S-TOH architectures to render HUY@S-TOH/AuPd materials.

To investigate the morphological evolution of the urchin-like architecture, experiments were conducted in the presence of different short-chain water-soluble alcohols. Our previous

research indicated that only etching processes take place in alkali water media and wrinkled TiO_2 spheres are obtained.³³ Herein, we further studied dissolution–renucleation and the growth process for Y@S TiO_2 microspheres. Therefore, the role of different water-soluble alcohols as a suitable agent for the dissolution–renucleation of titania materials for further morphology control was investigated.

Figure 1 displays SEM micrographs illustrating the subsequent integral urchin-like morphology evolution with different alcohols. As shown in **Figure 1a**, quasi-urchin-like structures of ultrathin needles were obtained in a methanol/water mixture. The use of ethanol instead of methanol led to well-defined hierarchical urchin-like architectures composed of thin needles (**Figure 1b**). The needles grew significantly, which indicates a better dissolution–renucleation process in the presence of ethanol.

The urchin-like structure was also retained using 1-propanol/water mixtures, but the lengths of the needles decreased at the expense of becoming wider (**Figure 1c**). Interestingly, the use of 2-propanol/water mixtures renders thicker and more compact needles, forming a chrysanthemum-like structure (**Figure 1d**), being even thicker and wider (peony-like structure) than that obtained for *tert*-butanol/water media mixtures (**Figure 1e**). In the presence of butanol as well as longer chain alcohols, urchin-like structures were not observed, indicating no dissolution–renucleation process is occurring using immiscible alcohols in water.

The formation process of an urchin-like yolk–shell superstructure can be explained by a “dissolution–re-nucleation” growth mechanism.^{36,37} TiO_2 can be etched from its exterior surfaces (due to reaction with NaOH) upon Y@S TiO_2 immersion in alkaline water/alcohol solution, generating sodium titanate. Subsequently, the generated sodium titanate reacts with alcohols to form alkoxy titanates. The produced alkoxy titanates are hydrolyzed in the presence of water and transformed into nuclei, with nanoneedles beginning to grow on the numerous nuclei existing on the surface of Y@S TiO_2 as a result of the hydrothermal treatment.

As is clear from **Figure 1** and also the results of **Table S1**, the most uniform urchin-like structure with higher surface area and activity is obtained in ethanol/water mixtures. Henceforth, HUY@S-TOH/AuPd nanoarchitectures, where the urchin-like morphology was prepared in ethanol/water media, are the focus for further characterization.

Figure 2 depicts SEM images of HUY@S-TOH/AuPd architectures at different magnification. As shown in **Figure 2a**, this structure has a spherical morphology with an interesting hierarchical urchin-like surface and a mean diameter of $\sim 3 \mu\text{m}$. The Y@S configuration can be confirmed by a movable core inside an urchin-like shell, as can be seen in the cracked structures (green arrows). **Figure 2b** depicts an SEM images of HUY@S-TOH/AuPd at high magnification which clearly shows the presence of hierarchically assembled needles on the surfaces of microspheres. As is clear from **Figure 2c** (broken shell), the shell interior is ultraporous, which is highly favorable for gas diffusion into the void space of the designed architecture, as confirmed by N_2 sorption and CO_2 adsorption analysis (see below).

Figure 3 shows TEM images of Y@S-TO, HUY@S-TOH, and HUY@S-TOH/AuPd architectures. **Figure 3** (a–c) clearly shows a hollow space between the inner core and outer shell, thus demonstrating a Y@S configuration in all structures. In contrast to the smooth surface of Y@S-TO (**Figure 3d**), TEM

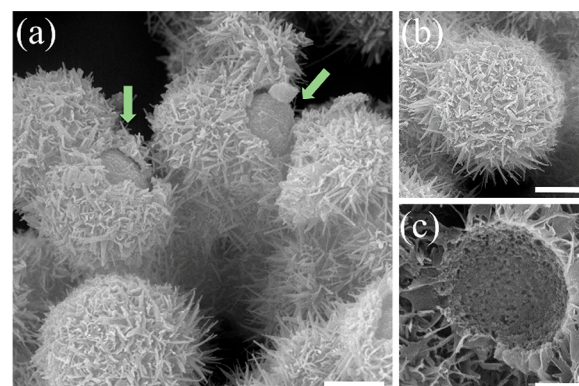


Figure 2. SEM images of the HUY@S-TOH/AuPd architectures. The scale bars are $1 \mu\text{m}$ (a–c).

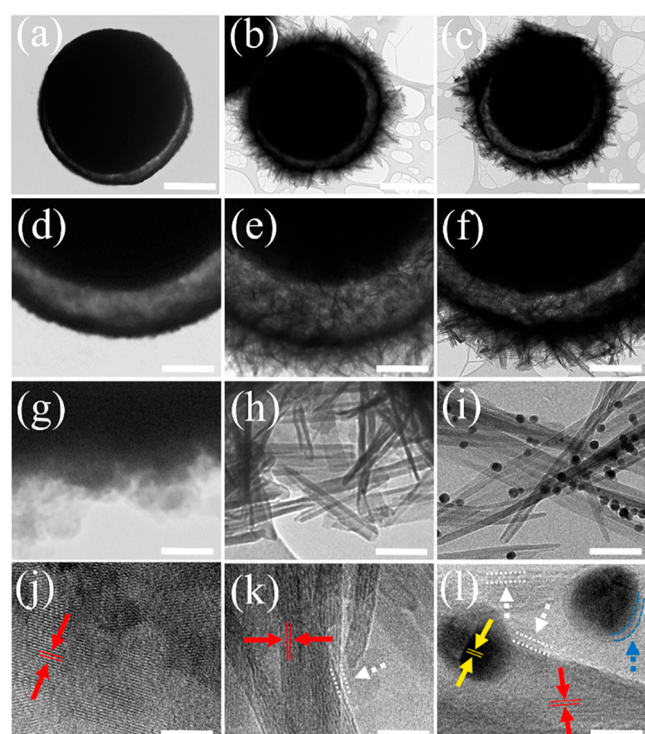


Figure 3. TEM (a–i) and HRTEM (j–l) images of the Y@S-TO, HUY@S-TOH, and HUY@S-TOH/AuPd architectures. The scale bars are $1 \mu\text{m}$ (a–c), 500 nm (d–f), 50 nm (g–i), and 5 nm (j–l).

images of HUY@S-TOH indicate a change of the surface from smooth to urchin-like after the dissolution–renucleation process in ethanol/water media (**Figure 3e**). The structure remained unchanged after hydrogen treatment and Au–Pd decoration in HUY@S-TOH/AuPd architecture (**Figure 3f**). High-magnification TEM images of the structures (**Figure 3g–i**) depict uniform needle decoration with Au–Pd nanoparticles in the HUY@S-TOH/AuPd architecture (**Figure 3i**). As shown in the HRTEM images (**Figure 3j–l**), all architectures exhibited a lattice spacing of 0.35 nm between (101) TiO_2 planes (red arrows). Moreover, a thin disordered surface layer could be imaged (white arrows) in **Figure 3** (k, l) that can be ascribed to the result of the hydrogenation process and the creation of Ti^{3+} ions on the surface of treated structures.¹⁸ Furthermore, Au–Pd nanoparticles are visible on the surface of needles with the interplanar spacing of ca. 0.24 nm (yellow arrows), which corresponds to the (111) planes of gold

nano particles (Figure 3l). The thin shell (blue lines, ca. 0.7 nm) that can be seen on the surface of Au particles corresponds to Pd, hence supporting the presence of core/shell Au–Pd nanoparticles as later on further confirmed by XPS (see below). HRTEM images evidence the intimate contact between the hydrogenated TiO₂ needles and Au–Pd core/shell nanoparticles.

XPS analysis was subsequently performed in order to learn more about the state of the different elements in HUY@S-TOH/AuPd architectures. Figure S1 shows the high-resolution XPS spectra for titanium (Ti 2p), oxygen (O 1s), gold (Au 4f), and palladium (Pd 3d). The spin orbit components (2p_{3/2} and 2p_{1/2}) of Ti 2p peak are presented in Figure S1a. After fitting, four Ti 2p peaks are obvious. The peaks at 464.9 and 459.0 eV can be assigned to the 2p_{1/2} and 2p_{3/2} core levels of Ti⁴⁺, whereas the peaks at 463.2 eV and 456.9 can be ascribed to the 2p_{1/2} and 2p_{3/2} core levels of Ti³⁺ in the hydrogenated TiO₂ lattice. Figure S1b indicates three peaks at 530.1, 532.2, and 533.9 eV corresponding to O₂⁻ species of Ti–O–Ti, oxygen atoms near the vacancies and chemisorbed oxygen species, respectively. The clearly notable peak at 532.1 eV confirms a high surface vacancy concentration in the HUY@S-TOH/AuPd structure.³⁸ Additionally, as shown in Figure S1c, the binding energy at 83.2 eV for Au 4f_{7/2} is consistent with the Au⁰ oxidation state, and the binding energy at 333.7 eV can be referred to Pd 3d_{5/2} in Pd⁰ oxidation state (Figure S1d). The weight amount of the Au and Pd determined by XPS in the HUY@S-TOH/AuPd architecture is ca. 2.3 and 0.6 wt %, respectively.

Interestingly, the peaks that were referenced to Pd 3d_{5/2} and Au 4f_{7/2} show a clear shift to lower binding energy compared to the typical binding energy for gold (Au⁰) and palladium (Pd⁰) at 84 and 335 eV, respectively (dashed lines in Figure S1). Moreover, a slight positive shift for Ti 2p_{3/2} is visible. These results can be referred to as the electron transfer from TiO₂/TiO_{2-x}H_x to Au–Pd, leading to electron-rich Au–Pd nanoparticles.^{39,40} The electron transfer clearly suggests the intimate contact between the HUY@S-TOH surface and the Au–Pd core/shell nanospheres. The electron flow toward the metal particles in the designed structure can considerably decrease the recombination rates of photogenerated charges. Moreover, the electron-rich state of the noble metal nanoparticles is favorable for CO₂ reduction.

The energy dispersive X-ray spectrometry (EDS) elemental mapping analysis was carried out to further confirm the elements in the HUY@S-TOH/AuPd architecture. As shown in Figure S2, this superstructure is composed of Ti, O, Au, and Pd elements with a homogeneous distribution.

Figure S3 shows the XRD patterns of Y@S-TO, HUY@S-TOH, and HUY@S-TOH/AuPd architectures. The reflections in the Y@S-TO sample are in good agreement with the normal reflections for the tetragonal anatase TiO₂ structure (JCPDS no. 21-1272). HUY@S-TOH exhibited an identical XRD pattern, with only a small shift observed toward higher angle, indicating the reduction of the interplanar distance of the TiO₂ crystalline phase as a result of the hydrogenation treatment.⁴¹ Two additional reflections can be observed after loading Au–Pd nanoparticles in HUY@S-TOH/AuPd as compared to HUY@S-TOH. A reflection at ~38° is referenced to (111) crystal faces of Au, in overlap with TiO₂ reflections, and a weak reflection at ~44° belongs to the (200) crystal face, indicating the crystalline structure for Au nanoparticles (JCPDS no. 10-0784). Nevertheless, the characteristic diffraction reflections

referenced to Pd were not detected, which indicates that the thickness of the deposited palladium shell on the surface of Au nanoparticles is beyond the detection limit for XRD analysis.⁴²

After structural analysis, the optical absorption properties were studied using UV–vis diffuse reflectance (DRS) analysis. Figure S4 displays the DRS spectra of HUY@S-TOH/AuPd in comparison to Y@S-TO and HUY@S-TOH structures. Y@S-TO exhibits only an absorption in the UV region whereas HUY@S-TOH reveals a strong absorption in the visible light range, as a result of structural changes during hydrogen treatment. After decoration with Au–Pd nanoparticles in the HUY@S-TOH/AuPd architecture, the visible-light absorption was strongly increased, indicating the high potential of HUY@S-TOH/AuPd architecture for visible light harvesting. Moreover, this structure exhibits a slight notable absorption centered at 532 nm which can be ascribed to the surface plasmon resonance effect of Au–Pd nanoparticles.³⁹

The photoluminescence (PL) of the Y@S-TO, HUY@S-TOH, and HUY@S-TOH/AuPd structures was studied. Since PL emission results from the recombination of electrons and holes, it is a helpful analysis to recognize the behavior of photogenerated electrons and holes in photocatalysts. As is clear from Figure S5, the PL intensity of the HUY@S-TOH decreased compared with Y@S-TO. This observation may be due to the formation of oxygen vacancies during the hydrogenation. The oxygen vacancies actually serve as electron traps and, hence, separate the charge carriers and reduce the recombination significantly. Moreover, the PL intensity of the HUY@S-TOH/AuPd was weaker than both that of Y@S-TO and HUY@S-TOH structures. This result indicates that the recombination rate of photogenerated electrons and holes is inhibited considerably in HUY@S-TOH/AuPd architectures, due to oxygen vacancies in the titanius part and also due to the Au/Pd nanoparticles.

Texture properties of Y@S-TO, HUY@S-TO, and HUY@S-TOH/AuPd structures were investigated by nitrogen physisorption as compared to commercial TiO₂ (C-TO). As shown in Figure S6, with the exception of C-TO which is not mesoporous, all samples exhibited type IV isotherms, revealing mesoporous features in these structures. Interestingly, HUY@S-TOH/AuPd possesses a large specific surface of 306 m² g⁻¹, which is close to that of HUY@S-TO (317 m² g⁻¹) and, importantly, much improved with respect to Y@S-TO (181 m² g⁻¹) and C-TO (41 m² g⁻¹). Moreover, the Barrett–Joyner–Halenda (BJH) pore size distribution results in Figure S7 indicate a narrow mesopore distribution in the range of 2–10 nm for HUY@S-TOH/AuPd. The high surface area and small pore size in the HUY@S-TOH/AuPd architecture can provide more active sites for CO₂ gas sorption in the designed nanostructure.

Since the diffusion and adsorption of CO₂ on the photocatalyst sites are the first critical steps in CO₂ photoreduction, the CO₂ adsorption ability was investigated for Y@S-TO, HUY@S-TO, and HUY@S-TOH/AuPd structures as compared to C-TO. As shown in Figure S8, except for nonporous C-TO, all other structures indicate a considerable CO₂ adsorption capacity. The HUY@S-TOH/AuPd structure exhibited a significant CO₂ adsorption capacity probably due to its urchin-like surface, inner hollow space, as well as defect sites produced during hydrogen treatment.

Photocatalytic CO₂ Reduction. Given the high surface area, robust CO₂ adsorption, strong visible light absorption, as well as intense electron-mediated transportations due to Au–



Figure 4. Comparison of CH_4 production rates of P25, P25/Au–Pd, Y@S-TO/AuPd, HUY@S-TOH/Au, HUY@S-TOH/Pd, and HUY@S-TOH/AuPd photocatalysts in the CO_2 reduction during 7 h.

Pd plasmonic nanoparticles, HUY@S-TOH/AuPd seems like an ideal photocatalyst for visible light reduction of CO_2 to solar fuels. Therefore, CO_2 photoconversion reactions were studied by CO_2 bubbling in water under visible light irradiation using a triple lined cylindrical glass reactor (Figure S9). The quantitative analysis was carried out using gas chromatography using an external standard through continuous sampling from the reactor. The background tests were performed in the absence of either photocatalyst, light, or CO_2 , and no hydrocarbons were detected. All hydrocarbon products were derived from CO_2 reduction under photoconversion.

The products of CO_2 photoreduction in water media using HUY@S-TOH/AuPd architecture are presented in Figure S10. As is clear from the results, the main hydrocarbon produced is CH_4 , whereas other possible CO_2 photoreduction products where much less observed and only CO was measured to $8 \mu\text{mol g}^{-1}$ after 7 h. The O_2 and H_2 evolution were also measured to 282 and $37 \mu\text{mol g}^{-1}$, respectively. These results indicate that the oxidation of water can be notably done along with CO_2 reduction in the presence of HUY@S-TOH/AuPd photocatalyst to provide the required species for CO_2 reduction (see also discussion of the mechanism later).

Moreover, to explore the role of visible light in this reaction, the photocatalytic activity of the HUY@S-TOH/AuPd structure was investigated using a Xe lamp equipped with a UV filter (>400 nm). As indicated in Figure S11, the CH_4 production when using a UV-cut filter did not decrease considerably. This observation underlines the fact that most of the photocatalytic activity of HUY@S-TOH/AuPd is in the visible spectral region due to the band gap position of the structure and also due to the plasmonic effect of AuPd nanoparticles.

Furthermore, CH_4 production did not considerably increase after 7 h during time-dependent reactions (Figure S12). Photocatalytic CH_4 production was considered for HUY@S-TOH/AuPd and benchmarked to P25, P25/Au–Pd, Y@S-TO/AuPd, HUY@S-TOH/Au, and HUY@S-TOH/Pd as reference photocatalysts during the 7 h. As is clear from the results shown in Figure 4, P25 displayed low activity in CO_2 photoreduction due to a low porosity and the missing visible light activity. Interestingly, the CH_4 production rate was significantly improved after decoration with Au–Pd nano-

particles on the structures, increasing to 72 and $84 \mu\text{mol g}^{-1}$ (after 7 h) using P25/AuPd and Y@S-TO/AuPd, respectively. The higher CH_4 evolution performance in the presence of Y@S-TO/AuPd can be ascribed to the higher surface area and larger CO_2 adsorption ability of Y@S-TO compared to P25, as previously measured by CO_2 sorption analysis. In the presence of monometallic photocatalysts, the CH_4 productions after 7 h were measured to 47 and $53 \mu\text{mol g}^{-1}$ for HUY@S-TOH/Au and HUY@S-TOH/Pd, respectively. This observation indicates that the presence of both Pd and Au plays an important role in this photocatalytic reaction. Interestingly, HUY@S-TOH/AuPd provided an optimum CH_4 production up to $126 \mu\text{mol g}^{-1}$ after 7 h, which is considerably higher as compared to that of any other materials. This notable activity of HUY@S-TOH/AuPd architecture for the photoconversion of CO_2 to CH_4 can be ascribed to rational modifications of this structure including (i) considerable absorption of CO_2 due to high porosity and hollow space in the Y@S urchin-like structure; (ii) improved visible light response as well as availability of excess electrons and adsorption sites for CO_2 and H_2O due to presence of oxygen vacancies on the surface of the structure; and (iii) enhanced charge separation and enriched electron transportation due to decoration of the structure with plasmonic Au–Pd nanoparticles.

To find the optimum loading ratio of Au–Pd nanoparticles on HUY@S-TOH, photocatalytic reactions were performed using different Au–Pd:HUY@S-TOH ratios (Figure S13). CH_4 production increases when the Au–Pd loadings increased from 1 to 3 wt %. No considerable improvements in CH_4 production rates were observed at higher metal loadings (over 3 wt %). These results indicated that the best loading of Au–Pd on the HUY@S-TOH structure is 3 wt %.

Figure 5 explains a plausible mechanism for the CO_2 photoreduction to CH_4 in the presence of HUY@S-TOH/AuPd photocatalyst, based on the catalytic experiments and characterization results (esp., XPS and DRS analysis). Under illumination, the connection between TiO_2 and $\text{TiO}_{2-x}\text{H}_x$, which have different band gaps (in the HUY@S-TOH part of the structure), can provide heterojunctions with a large amount of photogenerated electrons and holes.²⁶ The holes (h^+) remaining in the valence band can oxidize adsorbed water into the H^+ and O_2 that is required for the CO_2 conversion

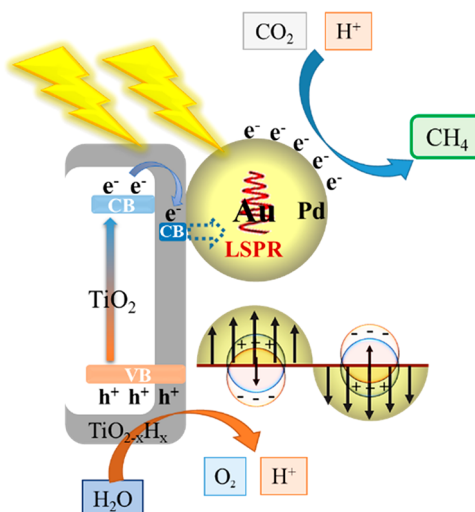


Figure 5. Schematic of the proposed mechanism for CO_2 photo-reduction by HUY@S-TOH/AuPd architecture.

reaction. The photoexcited electrons in the conduction band of TiO_2 can be transferred from the conduction band of $\text{TiO}_{2-x}\text{H}_x$ toward Au–Pd nanoparticles. Meanwhile, the illumination can produce hot e^- in Au nanoparticles, caused by LSPR, which can also be injected into the palladium shell.⁴³ These multiple flows of electrons can enrich the electron density of palladium to efficiently progress the CO_2 reduction reaction.

The photostability of the HUY@S-TOH/AuPd architectures was also estimated in six sequential reusability cycle tests. After each run, HUY@S-TOH/AuPd was centrifuged, washed several times with water, and dried under N_2 flow. As shown in Figure S14, the rate of CH_4 production remained almost unchanged without notable decrease during these tests, indicating an excellent photostability of engineered architectures during CO_2 conversion reaction. This stability can be ascribed to its robust architecture against chemical and structural collapse, as verified by XRD and TEM since all chemical and morphological structures of HUY@S-TOH/AuPd were almost fully preserved after reuses (Figure S14).

Finally, we compared the results of the photocatalytic CO_2 reduction to CH_4 with recent reports to explore the performance of the designed HUY@S-TOH/AuPd architecture. As shown in Table S2, our structure exhibits a remarkable CH_4 production as well as considerable stability in terms of reusability compared to most reported photocatalysts to date under similar reaction conditions.

CONCLUSIONS

HUY@S-TOH/AuPd architectures were designed through a multistep procedure that includes a solvothermal reaction toward Y@S-TO, which is an alkaline dissolution–renucleation process to design HUY@S-TO, and a high-temperature hydrogen treatment to achieve HUY@S-TOH/AuPd architecture, followed by decoration with prepared plasmonic Au–Pd core/shell nanoparticles on the surface of as-prepared structure. During the alkaline dissolution–renucleation process, the size and shape of the hierarchical needles of the urchin-like structure were tuned by adjusting the type of alcohols to achieve uniform urchin-like structures. The obtained yolk@shell urchin-like superstructure contains oxygen vacancies as well as abundant sharp needles that are decorated with Au–Pd

plasmonic nanoparticles. These structures exhibited production rates of up to $47 \mu\text{mol g}^{-1} \text{ h}^{-1}$ in the photocatalytic CO_2 reduction to CH_4 , which represents a much-improved performance as compared to benchmark photocatalysts. This considerable activity and selectivity of designed structure suggests that a balanced combination of porosity, surface defects, band position, and cocatalyst enables an efficient gas adsorption, visible light activation, charge recombination, and electron transportation to powerful CO_2 photoconversion. Our insight into the architectural engineering of this structure can serve as inspiration for the rational design of advanced photocatalysts, which can pave the way to further improve the energy conversion efficiency.

ASSOCIATED CONTENT

Supporting Information

The Supporting Information is available free of charge at <https://pubs.acs.org/doi/10.1021/acssuschemeng.9b06751>.

Experimental section, EDS mapping images, XRD patterns, DRS spectra, PL spectra, N_2 sorption, pore volume distribution, and CO_2 adsorption capacity of some of the structures, as well as the CO_2 photo-reduction products, time-dependent reaction, Au–Pd weight percentage influence, reusability study, and comparison of the efficiency of different photocatalysts in the CO_2 reduction to CH_4 (PDF)

AUTHOR INFORMATION

Corresponding Author

Thomas Burgi — Department of Physical Chemistry, University of Geneva, 1211 Geneva 4, Switzerland; orcid.org/0000-0003-0906-082X; Email: Thomas.Buergi@unige.ch

Authors

Abolfazl Ziarati — Department of Physical Chemistry, University of Geneva, 1211 Geneva 4, Switzerland; School of Chemistry, College of Science, University of Tehran, Tehran 1417614418, Iran

Ali Reza Badiei — School of Chemistry, College of Science, University of Tehran, Tehran 1417614418, Iran

Rafael Luque — Departamento de Química Orgánica, Universidad de Córdoba, E-14014 Córdoba, Spain; Peoples Friendship University of Russia (RUDN University), 117198 Moscow, Russia; orcid.org/0000-0003-4190-1916

Massoud Dadras — CSEM Centre Suisse d'Électronique et de Microtechnique SA, 2002 Neuchâtel, Switzerland

Complete contact information is available at: <https://pubs.acs.org/10.1021/acssuschemeng.9b06751>

Notes

The authors declare no competing financial interest.

ACKNOWLEDGMENTS

The authors thank the University of Tehran and the University of Geneva for supporting this work. A.Z. thanks Dr. Celine Besnard (Laboratory of Crystallography, University of Geneva) for X-ray measurements. The publication was prepared with support from the RUDN University Program 5-100.

REFERENCES

- (1) Artz, J.; Müller, T. E.; Thenert, K.; Kleinekorte, J.; Meys, R.; Sternberg, A.; Bardow, A.; Leitner, W. Sustainable conversion of

- carbon dioxide: An integrated review of catalysis and life cycle assessment. *Chem. Rev.* **2018**, *118* (2), 434–504.
- (2) Li, K.; Peng, B.; Peng, T. Recent advances in heterogeneous photocatalytic CO₂ conversion to solar fuels. *ACS Catal.* **2016**, *6* (11), 7485–7527.
- (3) Chen, D.; Zhang, X.; Lee, A. F. Synthetic strategies to nanostructured photocatalysts for CO₂ reduction to solar fuels and chemicals. *J. Mater. Chem. A* **2015**, *3* (28), 14487–14516.
- (4) Cai, X.; Hu, Y. H. Advances in catalytic conversion of methane and carbon dioxide to highly valuable products. *Energy Sci. Eng.* **2019**, *7* (1), 4–29.
- (5) Wang, C.; Sun, Z.; Zheng, Y.; Hu, Y. H. Recent progress in visible light photocatalytic conversion of carbon dioxide. *J. Mater. Chem. A* **2019**, *7* (3), 865–887.
- (6) Lee, Y. Y.; Jung, H. S.; Kang, Y. T. A review: Effect of nanostructures on photocatalytic CO₂ conversion over metal oxides and compound semiconductors. *Journal of CO₂ Utilization* **2017**, *20*, 163–177.
- (7) Xu, H.; Ouyang, S.; Liu, L.; Reunchan, P.; Umezawa, N.; Ye, J. Recent advances in TiO₂-based photocatalysis. *J. Mater. Chem. A* **2014**, *2* (32), 12642–12661.
- (8) Low, J.; Cheng, B.; Yu, J. Surface modification and enhanced photocatalytic CO₂ reduction performance of TiO₂: a review. *Appl. Surf. Sci.* **2017**, *392*, 658–686.
- (9) Habisreutinger, S. N.; Schmidt-Mende, L.; Stolarczyk, J. K. Photocatalytic reduction of CO₂ on TiO₂ and other semiconductors. *Angew. Chem., Int. Ed.* **2013**, *52* (29), 7372–7408.
- (10) Hu, H.; Lin, Y.; Hu, Y. H. Core-shell structured TiO₂ as highly efficient visible light photocatalyst for dye degradation. *Catal. Today* **2020**, *341*, 90–95.
- (11) Nakata, K.; Fujishima, A. TiO₂ photocatalysis: Design and applications. *J. Photochem. Photobiol., C* **2012**, *13* (3), 169–189.
- (12) Li, A.; Zhu, W.; Li, C.; Wang, T.; Gong, J. Rational design of yolk–shell nanostructures for photocatalysis. *Chem. Soc. Rev.* **2019**, *48* (7), 1874–1907.
- (13) Purbia, R.; Paria, S. Yolk/shell nanoparticles: classifications, synthesis, properties, and applications. *Nanoscale* **2015**, *7* (47), 19789–19873.
- (14) Ziarati, A.; Badiei, A.; Grillo, R.; Burgi, T. 3D Yolk@ Shell TiO_{2-x}/LDH Architecture: Tailored Structure for Visible Light CO₂ Conversion. *ACS Appl. Mater. Interfaces* **2019**, *11* (6), 5903–5910.
- (15) Liu, S.; Xia, J.; Yu, J. Amine-functionalized titanate nanosheet-assembled yolk@shell microspheres for efficient cocatalyst-free visible-light photocatalytic CO₂ reduction. *ACS Appl. Mater. Interfaces* **2015**, *7* (15), 8166–8175.
- (16) Li, X.; Yu, J.; Jaroniec, M. Hierarchical photocatalysts. *Chem. Soc. Rev.* **2016**, *45* (9), 2603–2636.
- (17) Reñones, P.; Moya, A.; Fresno, F.; Collado, L.; Vilatela, J. J.; de la Peña O’Shea, V. A. Hierarchical TiO₂ nanofibres as photocatalyst for CO₂ reduction: Influence of morphology and phase composition on catalytic activity. *Journal of CO₂ Utilization* **2016**, *15*, 24–31.
- (18) Chen, X.; Liu, L.; Yu, P. Y.; Mao, S. S. Increasing solar absorption for photocatalysis with black hydrogenated titanium dioxide nanocrystals. *Science* **2011**, *331* (6018), 746–750.
- (19) Naldoni, A.; Allieta, M.; Santangelo, S.; Marelli, M.; Fabbri, F.; Cappelli, S.; Bianchi, C. L.; Psaro, R.; Dal Santo, V. Effect of nature and location of defects on bandgap narrowing in black TiO₂ nanoparticles. *J. Am. Chem. Soc.* **2012**, *134* (18), 7600–7603.
- (20) Wang, Z.; Yang, C.; Lin, T.; Yin, H.; Chen, P.; Wan, D.; Xu, F.; Huang, F.; Lin, J.; Xie, X.; Jiang, M. H-doped black titania with very high solar absorption and excellent photocatalysis enhanced by localized surface plasmon resonance. *Adv. Funct. Mater.* **2013**, *23* (43), 5444–5450.
- (21) Pan, X.; Yang, M.-Q.; Fu, X.; Zhang, N.; Xu, Y.-J. Defective TiO₂ with oxygen vacancies: synthesis, properties and photocatalytic applications. *Nanoscale* **2013**, *5* (9), 3601–3614.
- (22) Yu, X.; Kim, B.; Kim, Y. K. Highly enhanced photoactivity of anatase TiO₂ nanocrystals by controlled hydrogenation-induced surface defects. *ACS Catal.* **2013**, *3* (11), 2479–2486.
- (23) Ji, Y.; Luo, Y. New mechanism for photocatalytic reduction of CO₂ on the anatase TiO₂ (101) surface: the essential role of oxygen vacancy. *J. Am. Chem. Soc.* **2016**, *138* (49), 15896–15902.
- (24) Xing, M.; Zhou, Y.; Dong, C.; Cai, L.; Zeng, L.; Shen, B.; Pan, L.; Dong, C.; Chai, Y.; Zhang, J.; Yin, Y. Modulation of the Reduction Potential of TiO_{2-x} by Fluorination for Efficient and Selective CH₄ Generation from CO₂ Photoreduction. *Nano Lett.* **2018**, *18* (6), 3384–3390.
- (25) Zhao, H.; Pan, F.; Li, Y. A review on the effects of TiO₂ surface point defects on CO₂ photoreduction with H₂O. *J. Materomics* **2017**, *3* (1), 17–32.
- (26) Sorcar, S.; Hwang, Y.; Grimes, C. A.; In, S.-I. Highly enhanced and stable activity of defect-induced titania nanoparticles for solar light-driven CO₂ reduction into CH₄. *Mater. Today* **2017**, *20* (9), 507–515.
- (27) Kar, P.; Farsinezhad, S.; Mahdi, N.; Zhang, Y.; Obuekwe, U.; Sharma, H.; Shen, J.; Semagina, N.; Shankar, K. Enhanced CH₄ yield by photocatalytic CO₂ reduction using TiO₂ nanotube arrays grafted with Au, Ru, and ZnPd nanoparticles. *Nano Res.* **2016**, *9* (11), 3478–3493.
- (28) Kermani, H.; Rohrbach, A. Orientation-Control of Two Plasmonically Coupled Nanoparticles in an Optical Trap. *ACS Photonics* **2018**, *5* (11), 4660–4667.
- (29) Yu, S.; Wilson, A. J.; Heo, J.; Jain, P. K. Plasmonic control of multi-electron transfer and C–C coupling in visible-light-driven CO₂ reduction on Au nanoparticles. *Nano Lett.* **2018**, *18* (4), 2189–2194.
- (30) Su, R.; Tiruvalam, R.; Logsdail, A. J.; He, Q.; Downing, C. A.; Jensen, M. T.; Dimitratos, N.; Kesavan, L.; Wells, P. P.; Bechstein, R.; et al. Designer titania-supported Au–Pd nanoparticles for efficient photocatalytic hydrogen production. *ACS Nano* **2014**, *8* (4), 3490–3497.
- (31) Yin, Z.; Wang, Y.; Song, C.; Zheng, L.; Ma, N.; Liu, X.; Li, S.; Lin, L.; Li, M.; Xu, Y.; et al. Hybrid Au–Ag nanostructures for enhanced plasmon-driven catalytic selective hydrogenation through visible light irradiation and surface-enhanced Raman scattering. *J. Am. Chem. Soc.* **2018**, *140* (3), 864–867.
- (32) Chen, Q.; Chen, X.; Fang, M.; Chen, J.; Li, Y.; Xie, Z.; Kuang, Q.; Zheng, L. Photo-induced Au–Pd alloying at TiO₂ {101} facets enables robust CO₂ photocatalytic reduction into hydrocarbon fuels. *J. Mater. Chem. A* **2019**, *7* (3), 1334–1340.
- (33) Ziarati, A.; Badiei, A.; Luque, R.; Ouyang, W. Designer hydrogenated wrinkled yolk@shell TiO₂ architectures towards advanced visible light photocatalysts for selective alcohol oxidation. *J. Mater. Chem. A* **2018**, *6* (19), 8962–8968.
- (34) Ziarati, A.; Badiei, A.; Luque, R. Black Hollow TiO₂ nanocubes: advanced nanoarchitectures for efficient visible light photocatalytic applications. *Appl. Catal., B* **2018**, *238*, 177–183.
- (35) Rohani, S.; Ziarati, A.; Ziarati, G. M.; Badiei, A.; Burgi, T. Engineering of Highly Active Au/Pd Supported on Hydrogenated Urchin-like Yolk@Shell TiO₂ for Visible Light Photocatalytic Suzuki Coupling. *Catal. Sci. Technol.* **2019**, *9*, 3820–3827.
- (36) Shao, F.; Sun, J.; Gao, L.; Yang, S.; Luo, J. Template-free synthesis of hierarchical TiO₂ structures and their application in dye-sensitized solar cells. *ACS Appl. Mater. Interfaces* **2011**, *3* (6), 2148–2153.
- (37) Bian, Z.; Zhu, J.; Li, H. Solvothermal alcoholysis synthesis of hierarchical TiO₂ with enhanced activity in environmental and energy photocatalysis. *J. Photochem. Photobiol., C* **2016**, *28*, 72–86.
- (38) Fan, J.; Cheng, L.; Liu, Y.; He, Y.; Wang, Y.; Li, D.; Feng, J. Insight into synergistic mechanism of Au@Pd and oxygen vacancy sites for coupling light-driven H₂O oxidation and CO₂ reduction. *J. Catal.* **2019**, *378*, 164–175.
- (39) Cybula, A.; Priebe, J. B.; Pohl, M.-M.; Sobczak, J. W.; Schneider, M.; Zielińska-Jurek, A.; Brückner, A.; Zaleska, A. The effect of calcination temperature on structure and photocatalytic properties of Au/Pd nanoparticles supported on TiO₂. *Appl. Catal., B* **2014**, *152*, 202–211.
- (40) Han, C.; Wu, L.; Ge, L.; Li, Y.; Zhao, Z. AuPd bimetallic nanoparticles decorated graphitic carbon nitride for highly efficient

reduction of water to H₂ under visible light irradiation. *Carbon* **2015**, *92*, 31–40.

(41) Xia, T.; Chen, X. Revealing the structural properties of hydrogenated black TiO₂ nanocrystals. *J. Mater. Chem. A* **2013**, *1* (9), 2983–2989.

(42) Wei, Y.; Jiao, J.; Zhao, Z.; Zhong, W.; Li, J.; Liu, J.; Jiang, G.; Duan, A. 3D ordered macroporous TiO₂-supported Pt@CdS core–shell nanoparticles: design, synthesis and efficient photocatalytic conversion of CO₂ with water to methane. *J. Mater. Chem. A* **2015**, *3* (20), 11074–11085.

(43) Zhang, S.; Chang, C.; Huang, Z.; Ma, Y.; Gao, W.; Li, J.; Qu, Y. Visible-light-activated Suzuki–Miyaura coupling reactions of aryl chlorides over the multifunctional Pd/Au/porous nanorods of CeO₂ catalysts. *ACS Catal.* **2015**, *5* (11), 6481–6488.